Journal of Materials Chemistry A

ROYAL SOCIETY OF CHEMISTRY

PAPER

View Article Online
View Journal | View Issue

Cite this: J. Mater. Chem. A, 2025, 13, 31421

Anion-rich solvation structures in high entropy aqueous electrolytes for supercapacitors with enlarged potential windows and superior rate capabilities

Laura González-Aguilera,[a] José Manuel Vicent-Luna,[b] Paula García-Balaguer,[a] Sofia Calero,[b] Rafael M. Madero-Castro,[c] Encarnación Raymundo-Piñero,[de] Xuejun Lu,[af] María C. Gutiérrez,[a] M. Luisa Ferrer *[a] and Francisco del Monte *[a]

The use of aqueous electrolytes as suitable electrolytes for supercapacitors (SCs) largely depends on maintaining a wide operating cell voltage window while ensuring good rate capabilities, thereby achieving high energy and power densities over many cycles. Electrolyte engineering with anion- and/or solvent-rich solvation structures has been recently explored in batteries of any type to enhance the interphase stability at high voltages, typically by the formation of a SEI. This approach has been less explored in SCs to not only extend the range of operational voltage but also balance the inherently distinct electrochemical stability of cations and anions with carbon electrodes. Herein, we prepared electrolytes composed of two ionic liquids with a common cation (*e.g.*, EMIMTFSI and EMIMBF$_4$) in solvent mixtures of H_2O, DMSO and CH_3CN. We found that the electrolyte with the richest solvation structure (*i.e.*, with many and diverse anions that surrounded the cation) was the most effective at widening the cell voltage at which the electrolyte is capable of operating (*e.g.*, up to 2.2 V). Interestingly, this extremely rich solvation structure also exhibited the best transport properties for different ions that, ultimately, were responsible for an excellent maintenance of the energy density at high power densities.

Received 12th June 2025
Accepted 7th August 2025

DOI: 10.1039/d5ta04796j

rsc.li/materials-a

1. Introduction

Electrolytes are lately playing a capital role in the optimization of electrochemical energy storage (EES) devices, from batteries of any type to supercapacitors (SCs).[1–6] Electrolytes are typically composed of salts (*e.g.*, regular ones and also ionic liquids, ILs) dissolved in water, organic solvents, or mixtures thereof. Pure ILs (without any further solvent) have also been used quite commonly taking advantage of their liquid nature. The choice of one type of electrolyte or another is essential for determining the main features of the EES device (*e.g.*, cell voltage, flammability, *etc.*). Aqueous electrolytes are affordable, safe and environmentally friendly. However, their electrochemical stability window (ESW) is limited to about 1–1.2 V due to electrolyte decomposition caused by the hydrogen evolution reaction (HER) and oxygen evolution reaction (OER) beyond this potential threshold. Organic electrolytes and ILs can achieve ESWs of up to 3.5–4 V, but they are costly and their high flammability and volatility pose significant safety and environmental risks. The challenge lies in finding safe and environmentally friendly aqueous-based electrolytes with large ESWs that provide high cell voltages.

In nature, the effect of relatively high content of various biological macromolecular components on different properties of proteins and nucleic acids *in vivo* (*e.g.*, folding mechanisms or conformational stability) is described as macromolecular crowding[7] in which the hydrogen bond (HB) structure of H_2O undergoes significant changes. Inspired by this phenomenon in living cells, several authors have applied the concept of molecular crowding to reduce the water activity in aqueous electrolytes and thus suppress water decomposition at voltages exceeding 1.6 V.[8–11] For instance, Xie *et al.* achieved this 'molecular crowding' in aqueous electrolytes by addition of high contents of water-miscible poly(ethylene glycol) (PEG) to an aqueous solution of LiTFSI so as to obtain LiTFSI : *x*PEG : (1

[a]Instituto de Ciencia de Materiales de Madrid-ICMM, Consejo Superior de Investigaciones Científicas-CSIC, Campus de Cantoblanco, 28049-Madrid, Spain. E-mail: delmonte@icmm.csic.es; mferrer@icmm.csic.es

[b]Materials Simulation and Modelling, Department of Applied Physics and Science Education, Eindhoven University of Technology, 5600MB Eindhoven, The Netherlands

[c]Department of Physical, Chemical, and Natural Systems, Universidad Pablo de Olavide, Ctra. Utrera km. 1, 41013 Seville, Spain

[d]CNRS, CEMHTI UPR3079, Univ. Orléans, 45071 Orléans, France

[e]Réseau sur le Stockage Électrochimique de l'Énergie (RS2E), 80039 Amiens Cedex, France

[f]State Key Laboratory of Chemical Resource Engineering, College of Chemical Engineering, Beijing University of Chemical Technology, Beijing 100029, P. R. China

− x)H_2O electrolytes with PEG content (x) ranging from 71% to 100%.[8]

However, the main characteristic of crowded systems in nature is not having one particular solute at a high concentration but reaching this high concentration by combining many different solutes whose individual concentrations are not really high. This idea somehow links with another emerging concept recently applied to pseudo-concentrated electrolytes, which is the increase of the configurational entropy of the systems that improves the compatibility of salts and solvents to form uniform solutions. This is typically achieved by the combination of multiple salts with a single solvent or/and a single salt with multiple solvents and results in such a diversity in the local interactions between solvents and ions that the solvation structure of ions becomes extremely complex. Non-aqueous high-entropy (HE) electrolytes have been widely used in Li[12–15] and Na[16–22] metal batteries. In these cases, the complex solvation structure obtained by anion and/or solvent enrichment not only stabilizes the electrode–electrolyte interphase but also improves cycling stability and rate performance. The design of aqueous HE electrolytes has been much less explored with most of the examples dealing with Zn-based electrolytes for Zn-ion batteries (ZIBs), dual-salt batteries and Zn-ion hybrid SCs (ZHSCs).[23–25] In these cases, the complex solvation structure was always modified with solvent molecules of different natures (*e.g.*, inert diluents, antisolvents, *etc.*) and it played the role of controlling the HER on the Zn anode, enhancing Zn^{2+} transport properties and facilitating Zn^{2+}-intercalation/deintercalation processes. More recently, the use of HE electrolytes in which the controlled addition of CH_3CN as a weak-coordinating solvent helped widen the operational voltage window with the subsequent improvement in the energy storage capabilities of SCs has been described.[26] Nevertheless, there is still a notable need in the field of SCs for studies exploring the formation of anion-rich solvation structures in aqueous HE electrolytes. Actually, chaotropic anions have been studied based on their capability to limit the fraction of free water in electrolytes.[27–30] However, the relationship between the anion-rich solvation structures of HE electrolytes with the ESW and the rate capability of SCs has not yet been fully addressed.

This work aimed to investigate whether balancing the ratio of two chaotropic anions with different sizes and hydrophilic/hydrophobic features (*e.g.*, BF_4^- and $TFSI^-$) may have a significant effect on the entropic features of the solvation structure of the electrolyte and, eventually, improve their electrochemical stability. Thus, we studied mixtures of two ILs sharing the cation (*e.g.*, EMIMTFSI and $EMIMBF_4$) dissolved in H_2O and some additional co-solvents, which were DMSO as a coordinating co-solvent and CH_3CN as a weak coordinating one. In particular, we studied mixtures of the type nEMIMBF$_4$: (1.5 − n)EMIMTFSI : $2H_2O$: DMSO : $1.5CH_3CN$, with n = 1.5, 1.15, 0.94, 0.69, 0.44, 0.2, and 0. The stoichiometry in which ILs and solvents were mixed was selected according to our previous experience with these types of solvent mixtures.[31,32] For instance, the deviations from ideality exhibited by liquid mixtures of H_2O and DMSO in different properties (viscosity, density, or enthalpy of mixing, among others) reached a maximum for the H_2O : DMSO mixture with a molar ratio of 2 : 1 (*e.g.*, $2H_2O$: DMSO). Meanwhile, the addition of CH_3CN to $2H_2O$: DMSO in molar ratios of 3.5 and above has typically resulted in flammable solvent mixtures.[26,33] So, in this work, the ternary liquid mixture of choice was $2H_2O$: DMSO : $1.5CH_3CN$ to avoid flammability issues. Moreover, this CH_3CN content provided the maximum deviation from ideality of density and viscosity in solvent mixtures with a single IL (*e.g.*, 1.5EMIMBF$_4$: $2H_2O$: DMSO : $1.5CH_3CN$).[33] Finally, the selected IL content provided solutions in the so-called "solvent-in-salt" regime.[33] The study of the nEMIMBF$_4$: (1.5 − n)EMIMTFSI : $2H_2O$: DMSO : $1.5CH_3CN$ mixtures included the analysis of the mixing behaviour of 1.5EMIMBF$_4$: $2H_2O$: DMSO : $1.5CH_3CN$ and 1.5EMIMTFSI : $2H_2O$: DMSO : $1.5CH_3CN$ by the determination of the excess of different properties (*e.g.*, density, viscosity and solvent donation) of the resulting mixtures. Moreover, the solvation structure was studied by different spectroscopic tools (NMR, ATR and NIR spectroscopy) and molecular dynamic (MD) simulations. In this regard, we obtained information about the formation or absence of HBs between ions and solvents, enabling us to evaluate the coordinating or non-coordinating nature of each one of the solvents and of the solvation structure of the electrolyte, more specifically of the cation that is common to both IL dilutions (*i.e.*, $EMIM^+$). Furthermore, electrochemical measurements were carried out for the determination of the structure–property-performance relationship of these complex electrolytes in SC cells using porous carbon materials as electrodes.

2. Deviations from ideality

As mentioned in the Introduction, our first objective was to investigate the mixing characteristics of nEMIMBF$_4$: (1.5 − n) EMIMTFSI : $2H_2O$: DMSO : $1.5CH_3CN$ mixtures (Table S1). For this purpose, our initial analysis focused on the deviation from ideality of the excess molar volumes, $V^E = (\chi_1 M_1 + \chi_2 M_2)/\rho - (\chi_1 M_1/\rho_1 + \chi_2 M_2/\rho_2)$, where M_1 and M_2 were the molecular weights of 1.5EMIMBF$_4$: $2H_2O$: DMSO : $1.5CH_3CN$ and 1.5EMIMTFSI : $2H_2O$: DMSO : $1.5CH_3CN$, respectively. We found negative deviations from ideality in a wide range of compositions (*i.e.*, for molar fractions of 1.5EMIMBF$_4$: $2H_2O$: DMSO : $1.5CH_3CN$ of *ca.* 0.7 and below, see Fig. 1a). Actually, mixtures of H_2O, DMSO and CH_3CN[34] and of hydrophilic salts based on $EMIM^+$,[35] including $EMIMBF_4$ in both DMSO and CH_3CN[36] and in mixtures of H_2O and DMSO,[19] have also exhibited negative values of excess molar volume. The occurrence of negative values of excess molar volume is usually associated with the formation of strong intermolecular interactions including charge transfer, dipole–dipole interactions, and HBs.[37] In our case, this volume contraction on mixing was maximum at n = 0.69 and could be ascribed to the interstitial accommodation of anions within a HB complex structure.

Previous studies have described that volume contractions on mixing coming from interstitial accommodation of solvent molecules within a HB complex structure are typically accompanied by the decrease of the melting point of the mixture.[38,39] In our case, the DSC scan of 1.5EMIMTFSI : $2H_2O$: DMSO : $1.5CH_3CN$ displayed a transition at −37 °C ascribed to the melting point of EMIMTFSI (Fig. 1b). Actually, the melting point

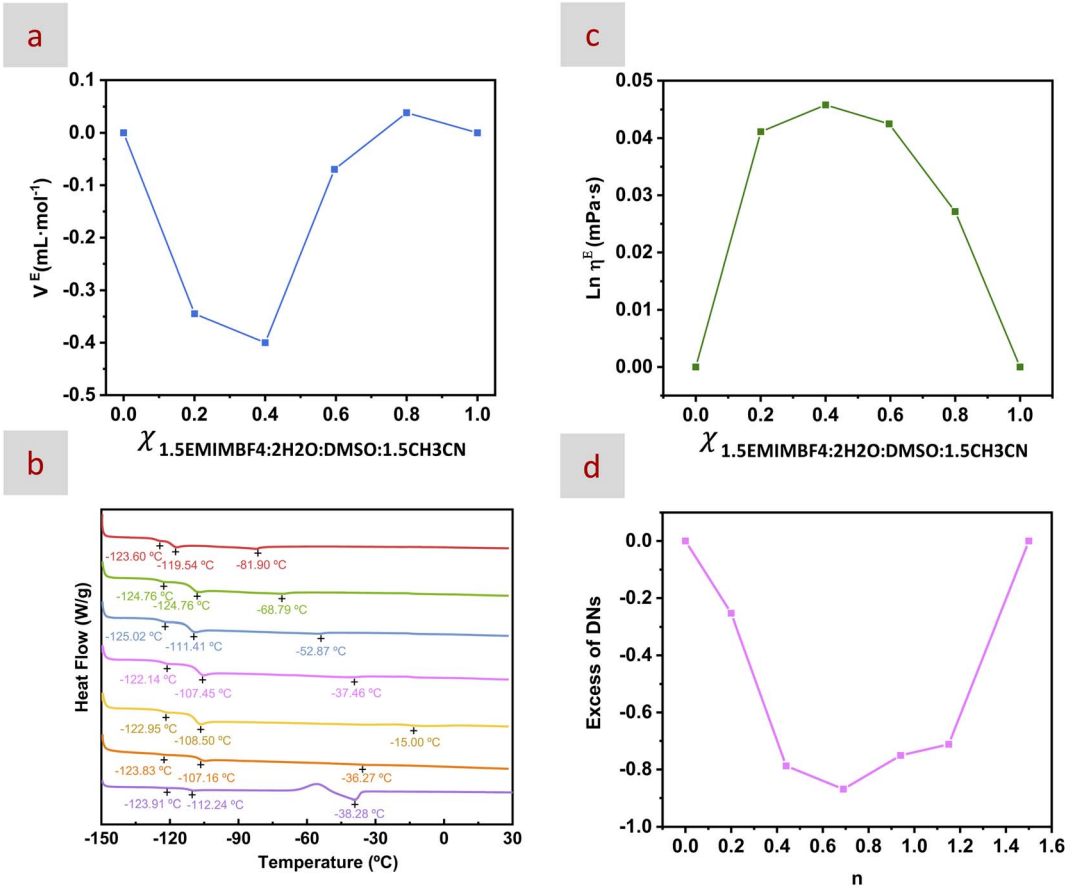

Fig. 1 Plots of (a) excess molar volume (V^E) and (c) excess logarithm viscosity ($\ln \eta^E$) *versus* $\chi_{1.5EMIMBF_4:2H_2O:DMSO:1.5CH_3CN}$ in mixtures of $1.5EMIMBF_4 : 2H_2O : DMSO : 1.5CH_3CN$ and $1.5EMIMTFSI : 2H_2O : DMSO : 1.5CH_3CN$. (b) DSC scans of $n EMIMBF_4 : (1.5 - n) EMIMTFSI : 2H_2O : DMSO : 1.5CH_3CN$ with $n = 1.5$ (red line), 1.15 (green line), 0.94 (blue line), 0.69 (pink line), 0.44 (yellow line), 0.2 (orange line) and 0 (purple line). (d) Plot of excess of donor numbers (DNs) as obtained from Fig. S1.

of EMIMTFSI in neat form (without solvents) appears at *ca.* −15 °C [40] and at *ca.* −23 °C in $1.5EMIMTFSI : 2H_2O : DMSO$.[26] None of the other samples studied in this work, neither the double IL mixtures nor the $EMIMBF_4$ mixture, displayed a clear melting point. This trend could be indicating that the $TFSI^-$ anion, despite its large size and hydrophobic nature, was interstitially accommodated within the HB complex structure formed by $EMIMBF_4$, H_2O, DMSO, and CH_3CN.

Moreover, every sample exhibited two weak glass transition temperatures (T_g), one at around −110 °C and another one at around −125 °C (Fig. 1b). The first T_g at around −110 °C has also been observed in mixtures of $EMIMBF_4$ and EMIMTFSI without solvents[39] while the second one at around −123 °C has been observed in mixtures of $H_2O : DMSO$ and of $H_2O : DMSO : CH_3CN$.[26] It is worth remembering that the absence of phase transitions such as melting points and crystallization processes is a typical signature of HE electrolytes so the decrease of the T_g could also be of relevance with regard to the eventual utilization of these electrolytes at low temperatures.

The positive deviations from ideality found in the representation of the excess logarithmic viscosity, obtained from the equation $\ln \eta^E = \ln \eta - (\chi_1 \ln \eta_1 + \chi_2 \ln \eta_2)$, corroborated the occurrence of HBs among the components of these mixtures (Fig. 1c)[41] that is typically accompanied by changes in the solvation structure.[42] Solute–solvent and solvent–solvent interactions in binary solvent mixtures were studied by ^{23}Na-NMR spectroscopy.[43,44] The deviation from ideality of the chemical shift of the ^{23}Na nucleus of dissolved $NaClO_4$ has been used for the determination of the donor numbers (DNs) defined by Gutmann.[45] The DN typically accounts for the electron donating properties (donicity) of solvent molecules but its use for ions has also been described.[46] Moreover, DNs may reflect the interaction between solvent molecules and ions as molecular fingerprints for the screening of electrolyte additives.[47] In our case, we found that the DNs of the $n EMIMBF_4 : (1.5 - n) EMIMTFSI : 2H_2O : DMSO : 1.5CH_3CN$ mixtures exhibited a non-linear evolution along with n, reaching a maximum deviation from ideality at $n = 0.69$ (Fig. S1 and 1d), as described above for densities and viscosities. Understanding whether this non-linear evolution in the DNs is associated with some specific changes in the solvation structure (*e.g.*, the so-called "preferential solvation")[44] would indeed be of interest. Further details about this matter can be found below (see discussion of the results from MD simulations).

3. The nature of the HB network

The mixtures were analyzed by ^{1}H NMR spectroscopy (Fig. S2). Increasing the content of EMIMTFSI caused slight downfield shifts (~0.02–0.04 ppm) in the aliphatic protons of $EMIM^+$ and DMSO, consistent with the more hydrophobic nature of $TFSI^-$ (as compared to BF_4^-) and its preferential interaction with aliphatic chains (Table S2).[48,49] Meanwhile, the H_2O proton signals shifted upfield as EMIMTFSI content increased from n = 1.5 to n = 0.94 and then downfield from n = 0.94 to 0. Deshielding, reflecting reduced electron density and stronger HB,[50,51] indicated that H_2O involvement in HB structures was lower in the nEMIMBF$_4$: (1.5 − n)EMIMTFSI : 2H_2O : DMSO : 1.5CH_3CN mixtures than in either 1.5EMIMBF$_4$: 2H_2O : DMSO : 1.5CH_3CN or 1.5EMIMTFSI : 2H_2O : DMSO : 1.5CH_3CN, reaching a minimum at n = 0.94. This reduction was attributed to the interstitial accommodation of incoming $TFSI^-$ anions. Meanwhile, $TFSI^-$ and BF_4^- signals (both $^{10}BF_4^-$ and $^{11}BF_4^-$ coming from J coupling between ^{19}F with ^{10}B, with spin I = 3 and *ca.* 20% of natural abundance, and ^{11}B nuclei, with spin I = 3/2 and *ca.* 80% of natural abundance)[52] followed a linear trend, with chemical shifts becoming more negative along with the decrease of n (Table S3).

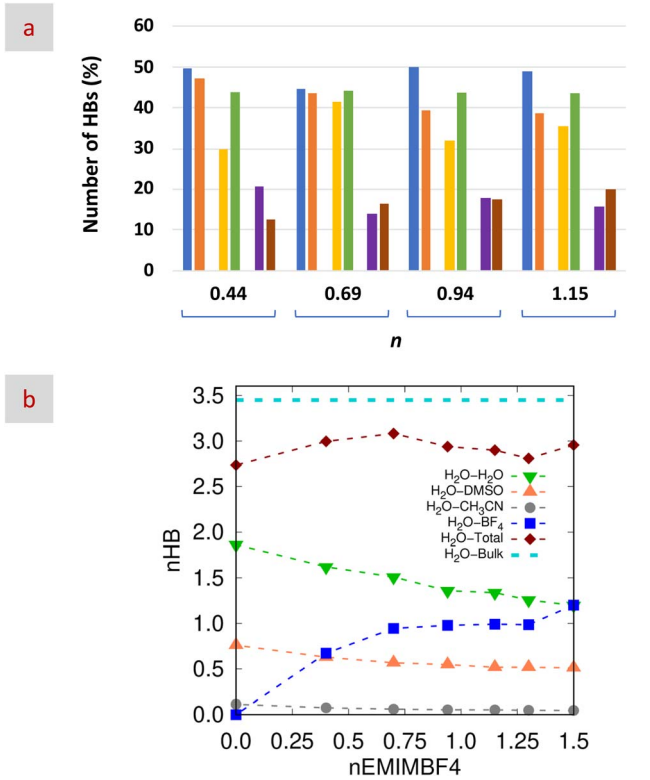

Fig. 2 (a) Number (in%) of strong (blue and orange bars), moderate (yellow and green bars) and weak (purple and brown bars) HBs obtained either by deconvolution of NIR spectra (blue, yellow and purple bars, see Table S4 for data) or from MD simulations (orange, green and brown bars) for nEMIMBF$_4$: (1.5 − n)EMIMTFSI : 2H_2O : DMSO : 1.5CH_3CN with n = 0.44, 0.69, 0.94, and 1.15. (b) Number of HBs (nHB) obtained from MD simulations for H_2O–H_2O (green triangles), H_2O–DMSO (orange triangles), H_2O–BF_4 (blue squares), and H_2O–CH_3CN (grey circles). The sum of all these HBs (red diamonds) and the number of HBs obtained for H_2O–H_2O in the bulk (dashed light blue line) are also included to estimate the "missing HBs". Data represented in (a) was obtained from the H_2O–H_2O values for strong HBs (orange bars), from the sum of H_2O–DMSO and H_2O–BF_4 for moderate HBs (green bars), and from the sum of H_2O–CH_3CN and "missing HBs" for weak HBs (brown bars).

ATR and NIR spectroscopies were used to analyze the mixtures. In the IR spectra (Fig. S4a), bands at *ca.* 3160, 3120, and 2960 cm^{-1} were attributed to ν(C4,5–H), ν(C2–H), and ν(alkyl C–H), respectively (Fig. S4b).[53] Key $TFSI^-$ features included SO_2 stretches (at *ca.* 1275–1400 cm^{-1}), CF_3 (at *ca.* 1194 cm^{-1}), and SNS (at *ca.* 1059 cm^{-1}). The asymmetric SO_2 stretch revealed free $TFSI^-$ anions at *ca.* 1355 cm^{-1} with a shoulder at *ca.* 1325 cm^{-1}, both shifting to lower wavenumbers upon coordination.[54] In our samples, these bands (at *ca.* 1355 and 1328 cm^{-1} for n = 1.15) shifted to smaller wavenumbers as $TFSI^-$ content increased (Fig. S4c). Additional bands assigned to BF_4^- appeared at *ca.* 997 and 1070 cm^{-1} with strong absorption, forming a broad single band (Fig. S4d).[55] Water bands at *ca.* 3407 and 3620 cm^{-1} (Fig. S4b) corresponded to molecules with strong (fully tetrahedral) and weak/incomplete HB, respectively.[56]

The NIR region further illuminated HB *via* overtone and combination bands. Water spectra were dominated by $\nu_2 + \nu_3$ (5100–5300 cm^{-1} → 1887–1941 nm) and $\nu_1 + \nu_3$ (6800–7200 cm^{-1} → 1389–1471 nm) combinations. These are derived from fundamental OH vibrations in the mid-infrared region (MIR),[57] such as the symmetric OH stretching (ν_1 at 3520 cm^{-1}), the OH bending (ν_2 at 1650 cm^{-1} → 6061 nm), and the antisymmetric OH stretching (ν_3 at 3600 cm^{-1} → 2778 nm).[58] Deconvolution of $\nu_2 + \nu_3$ revealed three components representing different HB strengths, from strong to weak, including an intermediate range of partially disordered tetrahedral structures.[59] In our case, the mixture at n = 0.69 showed the lowest contribution from strong HBs (Fig. S5 and Table S4). These NIR results were consistent with those of MD simulations (Fig. 2a and b), reinforcing the described features of the H_2O HB network (see further discussion below).

4. Anion-rich solvation structures

To further investigate the solvation structure in the mixtures, we analyzed the results from MD simulations. Initial analysis focused on the interactions between $EMIM^+$ nitrogen atoms and the most electronegative atoms of the other species, as reflected in the coordination number, cn(r), at *ca.* 6 Å in the partial radial distribution functions (pRDFs; Fig. S6). As n decreased, interactions with BF_4^- weakened, while those with $TFSI^-$ strengthened, showing a linear trend. Interactions with CH_3CN also slightly decreased. In contrast, H_2O and DMSO interactions peaked at n = 0.69, deviating from linear behavior.

Further insights were gained from trajectory analysis, which provided the average number of molecules (both solvents and anions) surrounding $EMIM^+$ in the first coordination shell as a function of n (Fig. 3). Solvent coordination numbers decreased with decreasing n, likely due to the incorporation of bulkier $TFSI^-$ anions (Fig. 3b). As expected, the presence of BF_4^- and

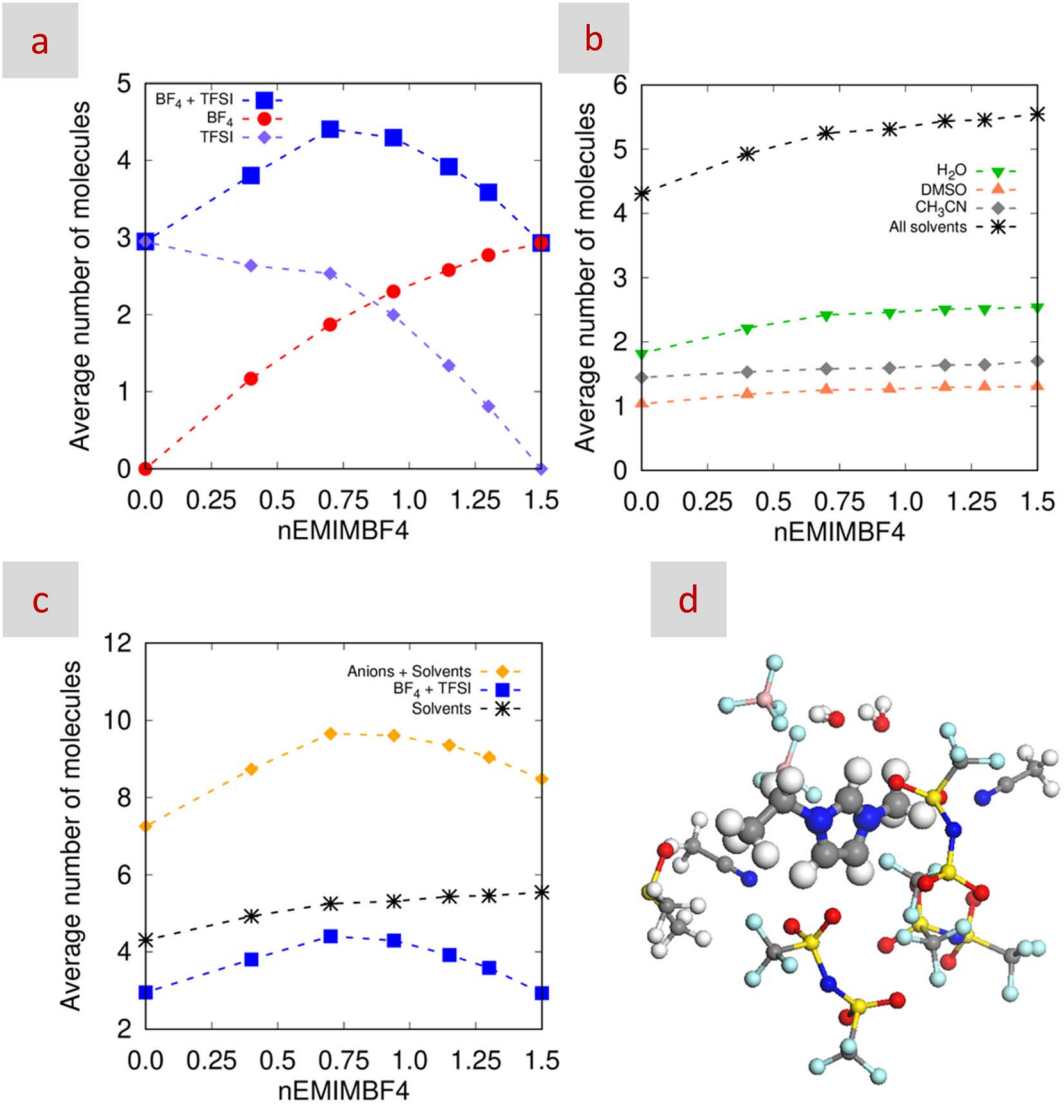

Fig. 3 Average number of (a) individual anions ($TFSI^-$ in purple, $BF4^-$ in red, and the sum in blue), (b) solvent molecules (H_2O in green, DMSO in orange, CH_3CN in grey, and the sum as black stars) and (c) the sum of ions (blue squares) and solvent molecules (black stars) surrounding $EMIM^+$ at distances lower than 6 angstroms *versus* *n*$EMIMBF_4$ for *n*$EMIMBF_4$: (1.5 − *n*)EMIMTFSI : $2H_2O$: DMSO : 1.5CH_3CN mixtures. (d) Snapshot of the *n*$EMIMBF_4$: (1.5 − *n*)EMIMTFSI : $2H_2O$: DMSO : 1.5CH_3CN mixtures with $n = 0.69$ that exhibited the $EMIM^+$–solvated complex with the highest coordination structure (above 9).

$TFSI^-$ followed opposing trends with *n* (Fig. 3a, red circles and purple diamonds, respectively). Notably, in single-salt mixtures and regardless of whether BF_4^- or $TFSI^-$ was present, the average number of anions surrounding $EMIM^+$ remained at *ca.* 3, as in neat $EMIMBF_4$ and EMIMTFSI.[60] While individual anion coordination did not reveal significant variation, summing the total number of anions around $EMIM^+$ did (Fig. 3a, blue squares). This total increased from *ca.* 3 for $n = 1.5$ or 0 to over 4 at $n = 0.94$ and 0.69, indicating a more complex solvation environment, especially at $n = 0.69$ (Fig. 3c and d). This supports the defining characteristic of HE electrolytes: an enhanced number and/or diversity of species in the first solvation shell compared to conventional (low-entropy) systems.

In order to investigate the accommodation of CH_3CN molecules, we analyzed the interactions between $EMIM^+$ and CH_3CN, that were weak according to the pRDF depicted in Fig. S6e. These results confirmed how CH_3CN participates in the solvation structure as a weak coordinating solvent disregarding its role as a non-coordinating one. Actually, FT-IR results from previous studies indicated that, as the CH_3CN content increases, the interactions among nitrogen atoms were strengthened to a greater extent than those among aliphatic groups.[48]

Finally, based on the positions of the first peak of the corresponding pRDFs, we found that both BF_4^- and $TFSI^-$ could form HBs with H_2O, noticeably stronger for BF_4^- than for $TFSI^-$.[61] Meanwhile, weak interactions were established between CH_3CN and CH_3CN (Fig. S7) as well as between any of the anions and any of the co-solvents (both DMSO and CH_3CN, see Fig. S8). HBs were also formed among the solvent

molecules, in particular between H_2O and H_2O, H_2O and DMSO, and H_2O and CH_3CN. Fig. S9 shows the pRDFs between the hydrogen atoms of water (acting as hydrogen bond donors, HBDs) and the electronegative atoms of H_2O, DMSO, and CH_3CN (oxygen atoms of DMSO and H_2O and the nitrogen atom of CH_3CN, acting as hydrogen bond acceptors, HBAs). Fig. S9 also shows the pRDFs between the oxygen atom of the HBD (*e.g.*, H_2O) with different HBAs. This set of pRDFs is commonly used to define the geometric criterion for HB formation[33,62–64] where the first minimum is located at *ca.* 3.5 Å for O–O/N pairs and 2.5 Å for H–O/N pairs. pRDFs in Fig. S8 and S9 revealed the formation of HBs of different strengths, strong between H_2O and H_2O, weak (almost negligible) between H_2O and CH_3CN, and moderate between H_2O and DMSO molecules and between H_2O and BF_4^- anions (Fig. 2b). Actually, the coordination numbers at the first minimum of the H_2O–H_2O and H_2O–DMSO pRDFs were basically unaffected by the formation of HBs between H_2O and CH_3CN. Interestingly, the total number of HBs obtained for the mixtures was below that obtained for bulk H_2O (*i.e.*, 2.75–3.0 and 3.45, respectively) thus revealing the occurrence of some "missing HBs". This is most likely happening when $TFSI^-$ and/or CH_3CN molecules (with which the HB formation is negligible), eventually driven by other type of interactions, are located in the proximity of H_2O molecules. It is worth noting that the number of strong, moderate and weak HBs obtained from MD simulations that formed the HB network established in the mixture was basically in agreement with that obtained from NIR spectroscopy (Fig. 2a).

5. Transport properties

As compared to regular low-entropy electrolytes, another characteristic of HE electrolytes is the increase in the ionic conductivity, eventually ascribed to the decrease of the cluster size of aggregates (AGGs).[12] In this regard, we studied the ionic conductivity of nEMIMBF$_4$: (1.5 − n)EMIMTFSI : 2H_2O : DMSO : 1.5CH_3CN mixtures and the diffusion coefficients of $EMIM^+$, BF_4^-, $TFSI^-$, H_2O, DMSO, and CH_3CN (*e.g.*, D_{EMIM^+}, $D_{BF_4^-}$, D_{TFSI^-}, D_{H_2O}, D_{DMSO}, and D_{CH_3CN}) from pulse-field-gradient spin-echo ^{19}F and ^1H NMR (PGSE-NMR) spectroscopy (Tables 1 and S5).

Ionic conductivity increased as viscosity decreased, that is, with increasing n. All diffusion coefficients were in the 10^{-10} m^2 s^{-1} range, consistent with the values reported for neat EMIMBF$_4$, EMIMTFSI,[60,65,66] and their dilutions in CH_3CN, H_2O, and H_2O : DMSO : CH_3CN mixtures (Table 1).[26,33,67,68] Ratios of D_{anion}/D_{cation} near unity suggest coupled ion motion,[69] indicative of AGGs (or contact ion pairs, CIPs), where ions diffuse together with other ions (and with solvent molecules in the particular case of CIPs).[70] According to the Stokes–Einstein relation ($D = k^BT/6\pi\eta a$), diffusion is inversely proportional to the hydrodynamic radius (a).[69,71] Thus, based on the Stokes–Einstein relation and the ionic sizes of BF_4^-, $EMIM^+$ and $TFSI^-$ (*e.g.*, 0.229, 0.303 and 0.528 nm, respectively), the expected order of self-diffusion coefficients should be $D_{BF_4^-} > D_{EMIM^+} > D_{TFSI^-}$.[66,72] This trend was observed in all mixtures except at n = 0.69, where $D_{EMIM^+} > D_{BF_4^-} > D_{TFSI^-}$. Transference numbers ($t_{EMIM^+}$, $t_{BF_4^-}$ and t_{TFSI^-}) followed the same trend, with $t_{BF_4^-} > t_{EMIM^+} > t_{TFSI^-}$ in all mixtures except at n = 0.69 where $t_{EMIM^+} > t_{BF_4^-}$ (Fig. 4a). Unlike Li-ion batteries, where high cation mobility is preferred, here the similar transference numbers across species (0.41–0.32 for $EMIM^+$, 0.39–0.32 for BF_4^-, and 0.30–0.26 for $TFSI^-$) support the efficient electric double-layer (EDL) mechanism dominant in SCs. In any case, for HE electrolytes, the hydrodynamic radius has been directly related to the cluster size of ionic AGGs, with high diffusivities of ions leading to small hydrodynamic radii and cluster sizes.[12,73–75] Interestingly, as mentioned above, every ion and every solvent molecule reached its respective highest diffusion at n = 0.69 (Fig. 4b), so, in our case, the smallest clusters would be found for this particular mixture.

We also estimated the molar conductivity ratio ($\Lambda : \Lambda_{NMR}$), where Λ is the molar conductivity obtained by electrochemical impedance measurements and Λ_{NMR} is that calculated from the ionic self-diffusion coefficients and the Nernst–Einstein equation.[71,76] It is widely assumed that, being the intrinsic NMR time scale (10^{-9} to 10^{-10} s) much shorter than those of the conductivity measurements, NMR measurements cannot distinguish ionic AGGs from free ions.[77] Thus, the $\Lambda : \Lambda_{NMR}$ ratio has been taken as an indication of the ionicity.[78] For instance, $\Lambda : \Lambda_{NMR}$ values below unity have been assigned to the presence of not only non-charged AGGs but also ionic ones.[78,79] In our case, the good ionicities obtained in the Walden plot depicted in Fig. S10 revealed the preferred presence of ionic AGGs.[71,80] Interestingly, the number of AGGs reached a maximum at n = 0.69 (Table 1). Considering that these values come from molar conductivities, the cluster size of the ionic AGGs formed in this latter mixture should be the smallest among all mixtures, as already anticipated by the above-mentioned relationship between the

Table 1 Diffusion coefficients of $EMIM^+$, BF_4^-, $TFSI^-$, H_2O, DMSO, and CH_3CN (*e.g.*, D_{EMIM^+}, $D_{BF_4^-}$, D_{TFSI^-}, D_{H_2O}, D_{DMSO}, and D_{CH_3CN}) obtained from ^{19}F (for BF_4^- and $TFSI^-$) and ^1H (for $EMIM^+$, H_2O, DMSO, and CH_3CN) NMR at 25 °C for nEMIMBF$_4$: (1.5 − n)EMIMTFSI : 2H_2O : DMSO : 1.5CH_3CN with n = 1.15, 0.94, 0.69, 0.44, and 0.2

	D (m^2 s^{-1}) × 10^{10}								
n	$EMIM^+$	BF_4^-	$TFSI^-$	DMSO	CH_3CN	H_2O	σ (mS cm^{-1})	Λ_{NMR} × 10^3 (S m^2 mol^{-1})	$\kappa = \Lambda/\Lambda_{NMR}$
1.15	2.88	3.03	2.23	3.73	6.18	7.59	39.6	7.1	0.25
0.94	2.48	2.95	2.33	3.27	5.67	6.74	35.6	6.2	0.27
0.69	4.02	3.18	2.59	4.87	7.61	8.12	31.2	7.8	0.20
0.44	2.46	2.82	1.95	3.09	5.82	6.45	28.1	5.0	0.29
0.2	1.58	1.54	1.15	1.90	3.85	4.42	25.3	2.9	0.48

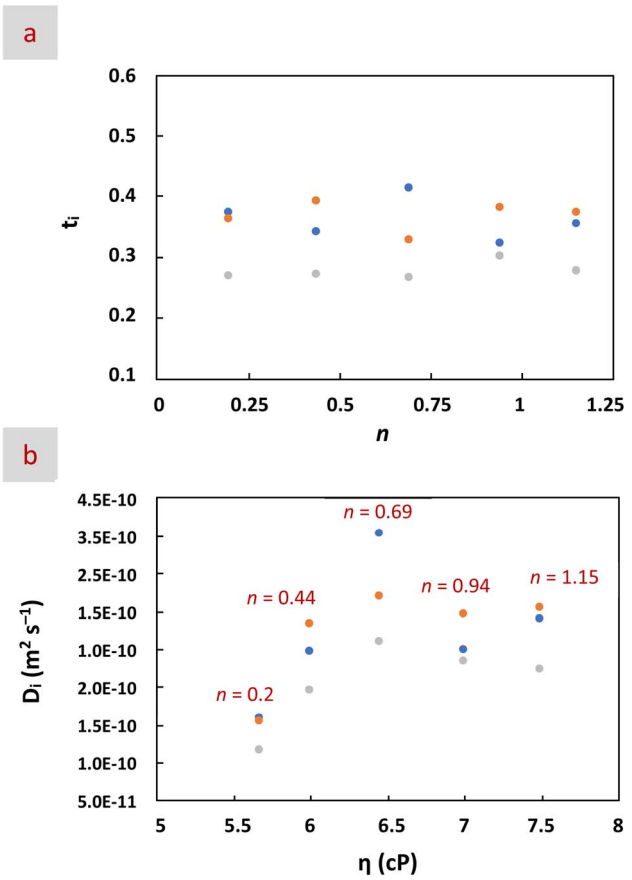

Fig. 4 (a) Plot of transference numbers of the cation $EMIM^+$ (t_{EMIM^+}, blue circles) and of the individual anions BF_4^- ($t_{BF_4^-}$, orange circles) and $TFSI^-$ (t_{TFSI^-}, grey circles) *versus* the molar BF_4^- content (*n*) in *n*EMIMBF$_4$: (1.5 − *n*)EMIMTFSI : 2H$_2$O : DMSO : 1.5CH$_3$CN mixtures, and (b) D_{EMIM^+} (blue circles), $D_{BF_4^-}$ (orange circles) and D_{TFSI^-} (grey circles) *versus* the viscosity (see Table S1) of *n*EMIMBF$_4$: (1.5 − *n*) EMIMTFSI : 2H$_2$O : DMSO : 1.5CH$_3$CN mixtures.

hydrodynamic radius and the diffusion coefficients. Moreover, as mentioned above, the formation of small clusters has been related to the entropic features of HE electrolytes.[12] In our case, as revealed by MD simulations, the mixture with $n = 0.69$ was particularly significant in this regard with a solvation structure with many and diverse anions and molecules around $EMIM^+$.

6. Electrochemical performance in SCs

At this stage, we proceeded to evaluate the electrochemical response of these mixtures in SC cells. For this purpose, Swagelok cells were assembled with two mesoporous carbons as electrodes and a 0.45 μm PVDF filter paper as a separator (see the Experimental section for further details).[33,81] The mesoporous carbons of choice were described in detail in our previous studies[31–33] and were selected based on their textural properties with a high surface area (*ca.* 2681 m^2 g^{-1}) and a large contribution of mesopores to the overall porosity with $V_{mesopores}$ above 70% of the total pore volume and an external surface area of *ca.* 500–650 m^2 g^{-1} (Fig. S11 and Table S6).

In SCs, the energy storage capability of any electrolyte is intimately related to its maximum operating cell voltage. For aqueous electrolytes, this is the voltage range between the highest potential at which irreversible oxidation occurs at the positive electrode (P_U) and the lowest potential at which hydrogen production occurs at the negative electrode (P_L). As these irreversible reactions are related to the ESW of the electrolyte, it is therefore that the determination of the ESW is of great interest. In this regard, the inherent distinct electrochemical stability of cations and anions with carbon electrodes creates an asymmetry in the potential of the positive and negative electrodes measured at zero voltage ($P_{0\ V}$), situating the $P_{0\ V}$ closer to P_U than to P_L and leaving some unused potential at the negative electrode.[82]

The determination of P_L, P_U, and $P_{0\ V}$ and of the potentials of both the negative and the positive electrodes (denoted as P_N and P_P, respectively) as a function of the operating voltage (V) was accomplished by the application of three-electrode procedures described elsewhere.[83] The determination of P_L and P_U is critical for the usefulness of an accurate estimation of the ESW. Thus, P_L and P_U are typically obtained from cyclic voltametry (CV) measurements in either a two- or a three-electrode set-up (Fig. S12–S15). Another option is performing chronoamperometric (CA) measurements at different potentials with a three-electrode set-up. Previous studies using CA categorized the so-called "safe potentials" for current densities below 0.1 A g^{-1} and/or above −10 μA cm^{-2}.[84,85] In our case, we investigated the samples for which the CA curves remained at current densities below 0.1 A g^{-1} for both positive and negative potentials.

Fig. 5 shows the CA curves obtained at potentials ranging from −0.8 to −1.6 V and from 0.6 to 1.2 V. The application of a threshold of 0.1 A g^{-1} for the "safe" regime resulted in potential limits (*e.g.*, [P_L, P_U]) of [−1.2, 0.9], [−1.3, 0.9], [−1.3, 0.9], [−1.3, 0.8], and [−1.3, 0.8] for the *n*EMIMBF$_4$: (1.5 − *n*) EMIMTFSI : 2H$_2$O : DMSO : 1.5CH$_3$CN mixtures with $n = 0.2$, 0.44, 0.69, 0.94, and 1.15 (see horizontal lines in red in Fig. 5). It was worth noting that the maximum voltage was limited by P_P, with the mixture with $n = 0.69$ performing the best, likely due to the distinct characteristics of its HB network (*i.e.*, see Fig. 1 and 2, with the mixture with $n = 0.69$ exhibiting, respectively, the maximum deviation from ideality in excess properties and the lowest number of weak HBs).

The analysis of Fig. 6 provided some useful information. First, the mixtures with $n = 0.2$ and 1.15 were disregarded as the best performing ones because the former exhibited narrower potential limits (*e.g.*, [−1.2, 0.9]) and the latter the highest unused potential at the negative electrode and the larger asymmetry between $P_{0\ V} - P_U$ and $P_{0\ V} - P_L$. Meanwhile, irreversible oxidation processes happened in the mixtures with $n =$ 0.44 and 0.94 at less positive potentials than in the mixture with $n = 0.69$. This latter mixture also exhibited the lowest unused potential at the negative electrode, so, overall, it was the best mixture balancing the distinct electrochemical stability of cations and anions. Moreover, according to the CV and CA

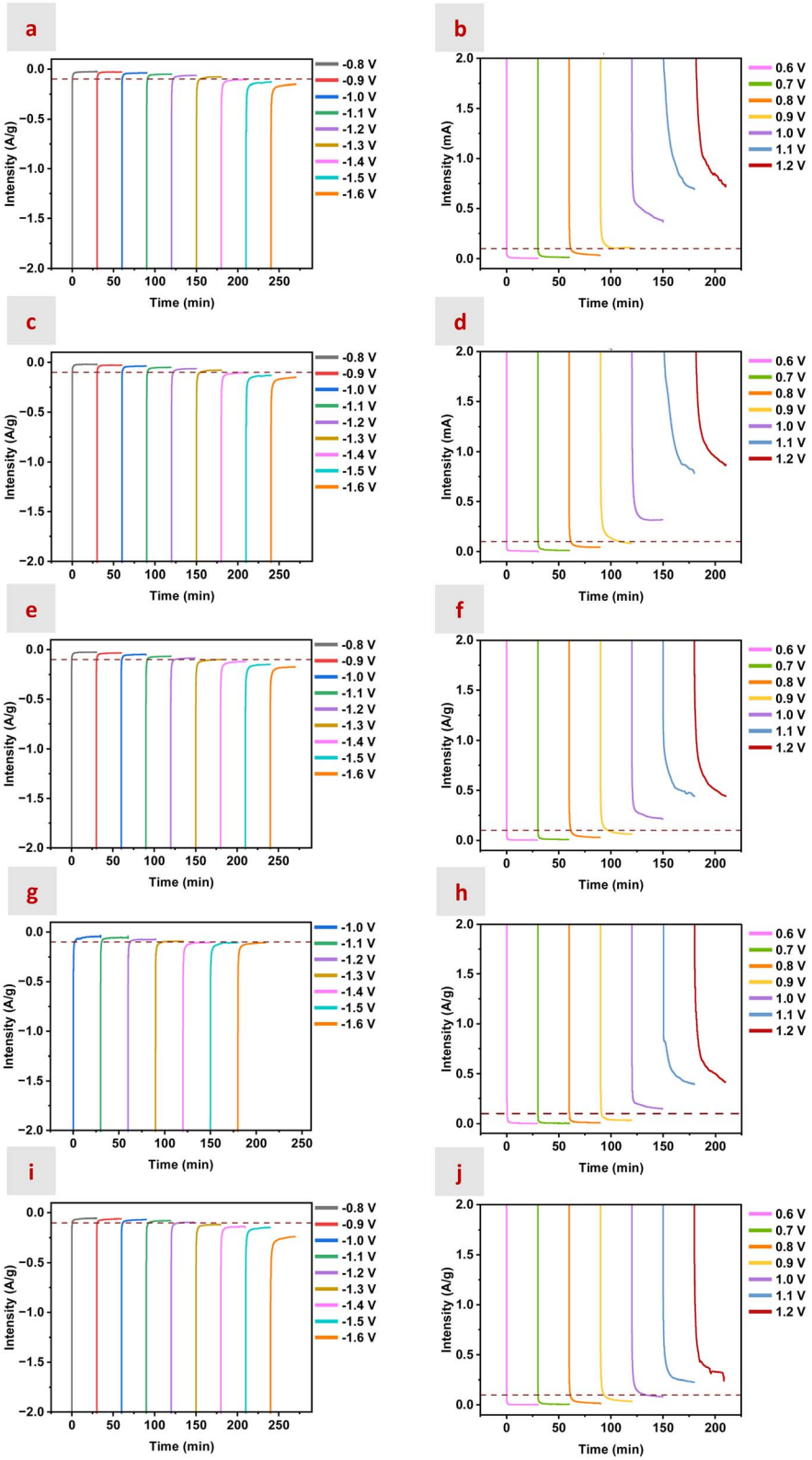

Fig. 5 Chronoamperometric curves at various applied negative (from −0.8 to −1.6, left column, a, c, e, g and i) and positive (from 0.6 to 1.2, right column, b, d, f, h and j) potentials obtained in a three-electrode configuration (*vs.* Ag/AgCl, 1 M KCl) using *n*EMIMBF$_4$: (1.5 − *n*)EMIMTFSI : 2H$_2$O : DMSO : 1.5CH$_3$CN, with $n = 1.15$ (a and b), 0.95 (c and d), 0.69 (e and f), 0.44 (g and h), and 0.2 (i and j), as electrolytes. Red lines at −0.1 and +0.1 A g^{-1} indicate the cutoff voltage for each system at, respectively, the negative and positive potentials for which the steady-state leak currents were considered negligible.

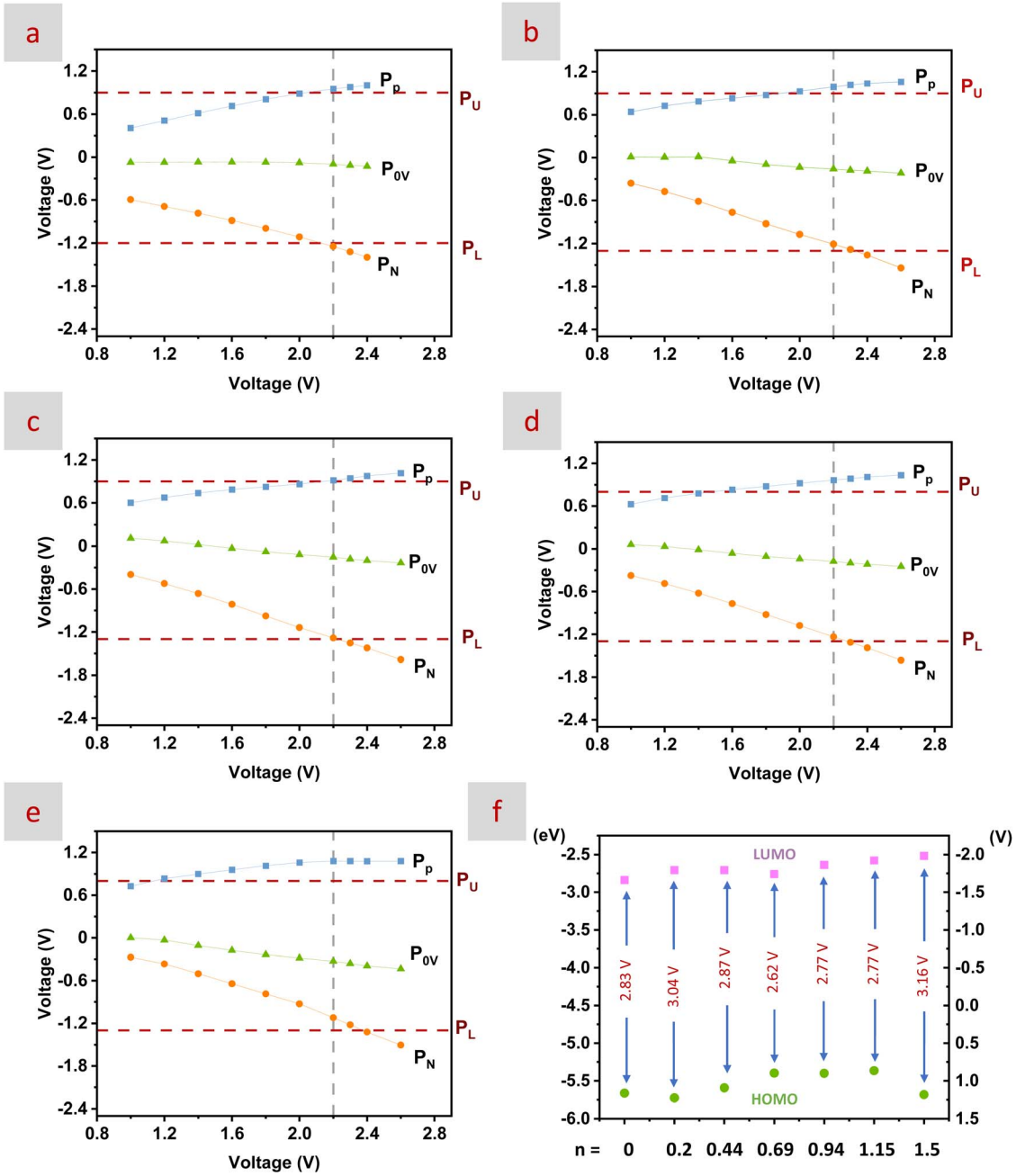

Fig. 6 Plot of the potentials reached by the positive (P_P, blue lines) and the negative electrodes (P_N, orange lines) during the operation of a two electrode cell using nEMIMBF$_4$: (1.5 − n)EMIMTFSI : 2H$_2$O : DMSO : 1.5CH$_3$CN mixtures, with n = 0.2 (a), 0.44 (b), 0.69 (c), 0.94 (d), and 1.15 (e), as electrolytes. The plot includes the potential of zero charge ($P_{0\,V}$, green lines) and the upper (P_U) and the lower (P_L) potential limits (see horizontal lines in red) for electrolyte decomposition. For an ESW of 2.2 V (see vertical lines in grey), the plot also illustrates the excess potential at the positive electrode ($P_P - P_U$) and the unused potential at the negative electrode ($P_N - P_L$). (f) HOMO–LUMO levels in eV (left y axis) and V (right y axis) obtained for nEMIMBF$_4$: (1.5 − n)EMIMTFSI : 2H$_2$O : DMSO : 1.5CH$_3$CN mixtures, with n = 0, 0.2, 0.44, 0.69, 0.94, 1.15, and 1.5.

measurements depicted above, the ESW of choice for subsequent experiments was 2.2 V.

Based on previous studies identifying the effective oxidation and reduction potentials of the electrolyte with the highest occupied molecular orbital (HOMO) and lowest unoccupied molecular orbital (LUMO) energy levels,[86,87] we also obtained the HOMO–LUMO energy levels of every mixture following the procedures described elsewhere.[88,89] In our case, the lowest LUMO and the narrowest HOMO–LUMO gap were found for the mixture with n = 0.69 (Fig. 6f). This pattern was opposite to that described in most of those previous studies mentioned above but in agreement with other studies describing how the reorganization and subsequent weakening of the interactions among the different components may cause the narrowing of the HOMO–LUMO energy gap.[90] Anyway, some authors have recently recommended abandoning the utilization of the

HOMO–LUMO energy levels when describing the electrolyte stability.[91]

Next, we performed electrochemical impedance spectroscopy (EIS) to begin with the assessment of the electrochemical performance of our mixtures (Fig. S16 and 7c). Despite the in-depth analysis of the results from EIS being rather complicated,[92,93] the Nyquist plot of an EDL capacitor measured in a two-electrode configuration typically displays some common features, which are a semicircle at high frequencies, followed by a nonvertical line at intermediate frequencies and then by a nearly vertical line at low frequencies. In this latter region, a slope of 90° is indicative of a purely capacitive system while the decrease of this angle reveals the presence of a charge transfer resistance in parallel to the EDL capacitance. Actually, the occurrence of such a decrease in the angle under the application of a certain potential has been used to study the electrode–electrolyte interphase and determine the cell voltage.[94–96] Moreover, the intersection of this nearly vertical line

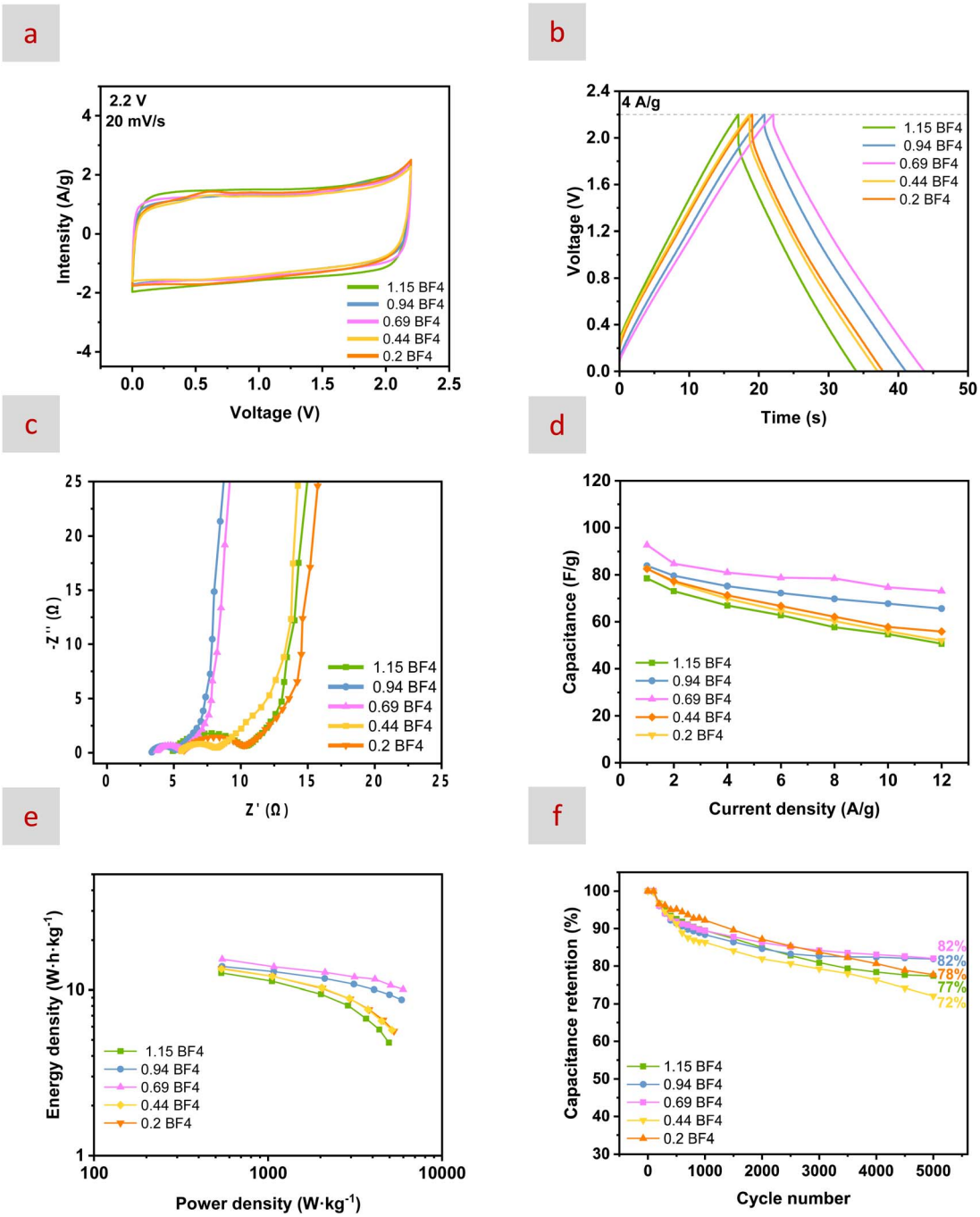

Fig. 7 CVs at 20 mV s^{-1} (a), GCDs at 4 A g^{-1} (b), Nyquist plots (c), the plot of capacitance *versus* current density (d), the Ragone plot (e) and capacitance retention upon cycling (f) obtained using *n*EMIMBF$_4$: (1.5−*n*)EMIMTFSI : 2H$_2$O : DMSO : 1.5CH$_3$CN mixtures with n = 1.15 (green lines), 0.95 (blue lines), 0.69 (pink lines), 0.44 (yellow lines), and 0.2 (orange lines), as electrolytes. The ESW was 2.2 V.

with the x axis provides the internal resistance (R_{int_EIS}, also named the equivalent series resistance, ESR)[93] of the cell. In our case, we observed how the mixture with $n = 0.69$ displayed the best performance overall, with both the lowest R_{int_EIS} (as compared to mixtures with $n = 1.15$, 0.44 and 0.2, Table S6) and the highest verticality (as compared to every mixture, including that with $n = 0.94$). Actually, the mixture with $n = 0.69$ exhibited the highest diffusion coefficients for every ion and the best balance among the diffusion transference numbers (Fig. 4) that, respectively, favour ion transport and help prevent charge accumulation and concentration gradients at the interface.

CV and galvanostatic charge/discharge (GCD) curves were also obtained for every mixture. CV was carried out at 25 °C and at scan rates ranging from 10 to 100 mV s^{-1} (Fig. S17). GCD curves were obtained at current densities ranging from 1 to 12 A g^{-1} (Fig. S18). The shape of both CV and GCD curves was typical of SCs, quasi-rectangular for CVs and near isosceles for GCDs (Fig. 7a and b). The shape of the CVs obtained at different potentials suggested that the most appropriate ESW for these mixtures was indeed 2.2 V. Interestingly, GCD curves revealed that the mixture with $n = 0.69$ was the best performing in terms of not only energy storage capabilities but also internal resistances (R_{int_IRdrop}, determined from the *IR* drop at the initiation of the current discharge for different current densities, Fig. S19 and Table S7).[97] As mentioned above for R_{int_EIS}, the internal resistance is directly influenced by the diffusion coefficients and transference numbers of the electrolyte. Considering that higher diffusion coefficients and well-balanced transference numbers (Fig. 4) led to lower internal resistance, faster charge transport and better performance, the mixture with $n = 0.69$ exhibited the best balance between energy and power density as observed in the plot representing specific capacitance *versus* current density and in the Ragone plot obtained for every mixture (Fig. 7d and e). Finally, the trend followed by the capacitance retentions obtained for the different mixtures after cycling 5000 times at 2.2 V and 3 A g^{-1} was basically the same as that described above for other electrochemical measurements, following the order $n = 0.69 \approx n = 0.94 > n = 0.2 \approx n = 1.15 > n = 0.44$ (Fig. 7f). The Nyquist plots obtained after cycling revealed different electrolyte deteriorations (Fig. S20), basically aligning with the above-observed capacitance retentions.

7. Conclusions

This work demonstrated how a proper combination of two chaotropic anions with different molecular sizes and hydrophilic/hydrophobic features promoted the formation of anion-rich solvation structures that helped balance the inherently distinct electrochemical stability of cations and anions in SCs. MD simulations allowed identifying the new arrangement of ions and solvent molecules happening in nEMIMBF$_4$: (1.5 − n)EMIMTFSI : 2H_2O : DMSO : 1.5CH_3CN mixtures for which the sum of BF_4^- and $TFSI^-$ anions in the first coordination shell outnumbers those of the single salt mixtures (*e.g.*, 1.5EMIMBF$_4$: 2H_2O : DMSO : 1.5CH_3CN or 1.5EMIMTFSI : 2H_2O : DMSO : 1.5CH_3CN). In particular, the number of anions around $EMIM^+$ increased from *ca.* 3 for both $n = 0$ and $n = 1.5$ to *ca.* 4.5 for $n = 0.69$ to obtain $EMIM^+$–solvated complexes in the form of a near-10-fold coordination structure (*e.g.*, $(BF_4^-)_a(TFSI^-)_b(EMIM^+)(H_2O)_c(DMSO)_d(CH_3CN)_e$, with $a + b = 4.5$ and $c + d + e = 5.2$). Spectroscopic analyses (ATR, NIR, and NMR) and MD simulations further confirmed that the HB network of H_2O at $n = 0.69$ is the weakest among all mixtures studied, consistent with the formation of a more disordered, loosely bound structure. This is corroborated by excess property analyses, which showed the greatest deviations from ideality at this composition, and by DN trends, which revealed a high level of complex solvent–solvent and solute–solvent interactions. All these results pointed to the formation of a loose structure that, as revealed by the diffusion coefficients obtained from PGSE-NMR spectroscopy, favours ion mobility minimizing charge accumulation and concentration gradients at the electrode–electrolyte interface. These structural and transport advantages translated directly into superior device performance: the electrolyte with $n = 0.69$ delivered the lowest internal resistance values (confirmed by both Nyquist plots and *IR* drops from GCD curves) and the best rate capability among all tested systems. This is particularly notable given the demanding nature of rate performance in SCs, more so than that needed in Li- or Na-metal ion batteries. In summary, the findings demonstrate that HE electrolytes with carefully tuned anion-rich solvation structures (with the mixture with $n = 0.69$ as the most remarkable example) can simultaneously improve energy storage and power delivery in SCs, positioning them as a promising candidate for next-generation energy storage systems.

8. Experimental section

The details of the sample preparation and the details of all the measurements and simulations are described in the SI.

Conflicts of interest

The authors have no conflicts of interest.

Data availability

Data for this article, including data presented in figures and tables have been included as part of the SI.

Experimental procedures, tables with different data (physicochemical properties, NMR chemical shifts, *etc.*), NMR, ATR and NIR spectra, RDFs from MD simulations, and electrochemical results (CVs, GCDs, Nyquist plots, *etc.*). See DOI: https://doi.org/10.1039/d5ta04796j.

Acknowledgements

This work was supported by MCIN/AEI/10.13039/501100011033 (TED2021-130372B-C42, TED2021-131812B-I00 and PID2021-123648OB-I00), by "ERDF A way of making Europe" (PID2021-123648OB-I00) and by "European Union Next Generation EU/PRTR" (TED2021-130372B-C42 and TED2021-131812B-I00). Authors also acknowledge the Severo Ochoa Centres of

Excellence Program through Grant CEX2024-001445-S. L. G.-A. acknowledges the grant PRE2019-090008 funded by MCIN/AEI/10.13039/501100011033 and "ESF Investing in your future". P. G.-B. acknowledges the grant PRE2022-101750 funded by MCIN/AEI/10.13039/501100011033 and ESF+. X. L. also acknowledges the National Natural Science Foundation of China (22393961). J. M. V.-L., S. C., and R. M. M.-C. also thank C3UPO for HPC support. The Servicio Interdepartmental de Investigación (SIdI) of the Universidad Autónoma de Madrid and the Thermal Analysis Unit at the Instituto de Ciencia de Materiales de Madrid (ICMM) are acknowledged for helpful assistance with FTIR and NMR spectroscopies and DSC studies, respectively.

References

1 M. Armand and J.-M. Tarascon, *Nature*, 2008, **451**, 652–657.
2 A. S. Aricò, P. Bruce, B. Scrosati, J.-M. Tarascon and W. van Schalkwijk, *Nat. Mater.*, 2005, **4**, 366–377.
3 T. S. Mathis, N. Kurra, X. Wang, D. Pinto, P. Simon and Y. Gogotsi, *Adv. Energy Mater.*, 2019, **9**, 1902007.
4 Z. Lin, E. Goikolea, A. Balducci, K. Naoi, P. L. Taberna, M. Salanne, G. Yushin and P. Simon, *Mater. Today*, 2018, **21**, 419–436.
5 C.-C. Chen and J. Maier, *Nat. Energy*, 2018, **3**, 102–108.
6 M. Chen, G. Feng and R. Qiao, *Curr. Opin. Colloid Interface Sci.*, 2020, **47**, 99–110.
7 L. A. Ferreira, V. N. Uversky and B. Y. Zaslavsky, *Mol. BioSyst.*, 2017, **13**, 2551–2563.
8 J. Xie, Z. Liang and Y.-C. Lu, *Nat. Mater.*, 2020, **19**, 1006–1011.
9 D. Dong, J. Xie, Z. Liang and Y.-C. Lu, *ACS Energy Lett.*, 2022, **7**(1), 123–130.
10 D. E. Ciurduc, C. de la Cruz, N. Patil, A. Mavrandonakis and R. Marcilla, *Energy Storage Mater.*, 2022, **53**, 532–543.
11 Q. Nian, W. Zhu, S. Zheng, S. Chen, B.-Q. Xiong, Z. Wang, X. Wu, Z. Tao and X. Ren, *ACS Appl. Mater. Interfaces*, 2021, **13**, 51048–51056.
12 S. C. Kim, J. Wang, R. Xu, P. Zhang, Y. Chen, Z. Huang, Y. Yang, Z. Yu, S. T. Oyakhire, W. Zhang, L. C. Greenburg, M. S. Kim, D. T. Boyle, P. Sayavong, Y. Ye, J. Qin, Z. Bao and Y. Cui, *Nat. Energy*, 2023, **8**, 814–826.
13 F. Cheng, W. Zhang, Q. Li, C. Fang, J. Han and Y. Huang, *ACS Nano*, 2023, **17**, 24259–24267.
14 Q. Wang, C. Zhao, J. Wang, Z. Yao, S. Wang, S. G. H. Kumar, S. Ganapathy, S. Eustace, X. Bai, B. Li and M. Wagemaker, *Nat. Commun.*, 2023, **14**, 440.
15 Q. Wang, C. Zhao, F. Wu, S. G. H. Kumar, S. Ganapathy, S. Eustace, X. Bai, B. Li, J. Lu and M. Wagemaker, *Adv. Mater.*, 2023, **35**, 2210677.
16 M. Mao, X. Ji, Q. Wang, Z. Lin, M. Li, T. Liu, C. Wang, Y.-S. Hu, H. Li, X. Huang, L. Chen and L. Suo, *Nat. Commun.*, 2023, **14**, 1082.
17 F. Hu, J. Chen, H. Cao, H. Wang, H. Guo and X. Ouyang, *Adv. Funct. Mater.*, 2025, **35**, 2413004.
18 C. Yang, X. Liu, Y. Lin, L. Yin, J. Lu and Y. You, *Adv. Mater.*, 2023, **35**, 2301817.
19 B. Ge, J. Deng, Z. Wang, Q. Liang, L. Hu, X. Ren, R. Li, Y. Lin, Y. Li, Q. Wang, B. Han, Y. Deng, X. Fan, B. Li, G. Chen and X. Yu, *Adv. Mater.*, 2024, **36**, 2408161.
20 Y. Zou, B. Zhang, H. Luo, X. Yu, M. Yang, Q. Zheng, J. Wang, C. Jiao, Y. H. Chen, H. Zhang, J. Xue, X. Kuai, H.-G. Liao, C. Ouyang, Z. Ning, Y. Qiao and S.-G. Sun, *Adv. Mater.*, 2024, **36**, 2410261.
21 H. Lohani, A. Kumar, A. Bano, A. Ghosh, P. Kumari, A. Ahuja, A. Sengupta, D. Kumar, D. T. Major and S. Mitra, *Adv. Energy Mater.*, 2024, **14**, 2401268.
22 Z. Cheng, Z. Zhang, F. Qiu, Z. Gao, H. Xie, Z. Xu, M. Jia, X. Zhang and H. Zhou, *ACS Energy Lett.*, 2025, **10**, 177–184.
23 C. Yang, J. Xia, C. Cui, T. P. Pollard, J. Vatamanu, A. Faraone, J. A. Dura, M. Tyagi, A. Kattan, E. Thimsen, J. Xu, W. Song, E. Hu, X. Ji, S. Hou, X. Zhang, M. S. Ding, S. Hwang, D. Su, Y. Ren, X.-Q. Yang, H. Wang, O. Borodin and C. Wang, *Nat. Sustain.*, 2023, **6**, 325–335.
24 J. Hao, L. Yuan, C. Ye, D. Chao, K. Davey, Z. Guo and S.-Z. Qiao, *Angew. Chem., Int. Ed.*, 2021, **60**, 7366–7375.
25 X. Liang, Y. Liang, Y. Gao, W. Qiao, D. Yin, P. Huang, C. Wang, L. Wang and Y. Cheng, *Small*, 2024, **20**, 2408162.
26 L. González-Aguilera, J. M. Vicent-Luna, S. Tao, S. Calero, R. M. Madero-Castro, E. Raymundo-Piñero, X. Lu, M. C. Gutiérrez, M. L. Ferrer and F. del Monte, *Adv. Funct. Mater.*, 2024, **34**, 2400337.
27 K. I. Assaf and W. M. Nau, *Angew. Chem., Int. Ed.*, 2018, **57**, 13968–13981.
28 D. Reber, R. Grissa, M. Becker, R.-S. Kühnel and C. Battaglia, Anion Selection Criteria for Water-in-Salt Electrolytes, *Adv. Energy Mater.*, 2021, **11**, 2002913.
29 Z. A. Zafar, G. Abbas, K. Knizek, M. Silhavik, P. Kumar, P. Jiricek, J. Houdková, O. Frank and J. Cervenka, *J. Mater. Chem. A*, 2022, **10**, 2064–2074f.
30 A. Tot, L. Zhang, E. J. Berg, P. H. Svensson and L. Kloo, *Sci. Rep.*, 2023, **13**, 2154.
31 X. Lu, R. J. Jiménez-Riobóo, D. Leech, M. C. Gutiérrez, M. L. Ferrer and F. del Monte, *ACS Appl. Mater. Interfaces*, 2020, **12**, 29181–29193.
32 X. Lu, J. M. Vicent-Luna, S. Calero, M. J. Roldán-Ruiz, R. Jiménez, M. L. Ferrer, M. C. Gutiérrez and F. del Monte, *ChemSusChem*, 2020, **13**, 5983–5995.
33 X. Lu, J. M. Vicent-Luna, S. Calero, R. M. Madero-Castro, M. C. Gutiérrez, M. L. Ferrer and F. del Monte, *Energy Storage Mater.*, 2021, **40**, 368–385.
34 H. A. Zarei, M. Z. Lavasani and H. Iloukhani, *J. Chem. Eng. Data*, 2008, **53**, 578–585.
35 C. A. Hall, K. A. Le, C. Rudaz, A. Radhi, C. S. Lovell, R. A. Damion, T. Budtova and M. E. Ries, *J. Phys. Chem. B*, 2012, **116**, 12810–12818.
36 O. Iulian and O. Ciocirlan, *J. Chem. Eng. Data*, 2012, **57**, 2640–26646.
37 E. J. González, L. Alonso and A. Domínguez, *J. Chem. Eng. Data*, 2006, **51**(4), 1446–1452.
38 V. Agieienko and R. Buchner, *J. Chem. Eng. Data*, 2019, **64**, 4763–4774.
39 V. Agieienko and R. Buchner, *J. Chem. Eng. Data*, 2020, **65**, 1900–1910.

40 C. L. Bentley, M. Y. Balogun, O. Morales-Collazo and J. F. Brennecke, *J. Chem. Eng. Data*, 2024, **69**(10), 3532–3543.
41 H. Zhang, X. Lu, L. González-Aguilera, M. L. Ferrer, F. del Monte and M. C. Gutiérrez, *J. Chem. Phys.*, 2021, **154**, 184501.
42 N. López-Salas, J. M. Vicent-Luna, S. Imberti, E. Posada, M. J. Roldán, J. A. Anta, S. R. G. Balestra, R. M. Madero Castro, S. Calero, R. J. Jiménez-Riobóo, M. C. Gutiérrez, M. L. Ferrer and F. del Monte, *ACS Sustainable Chem. Eng.*, 2019, **7**, 17565–17573.
43 A. R. Harifi-Mood, F. Sharifi and H. R. Bijanzadeh, *ChemistrySelect*, 2021, **6**, 600–608.
44 J. Catalán, C. Díaz and F. García-Blanco, *J. Org. Chem.*, 2000, **65**, 9226–9229.
45 M. Schmeisser, P. Illner, R. Puchta, A. Zahl and R. van Eldik, *Chem.–Eur. J.*, 2012, **18**, 10969–10982.
46 R. Younesi, G. M. Veith, P. Johansson, K. Edstro and T. Veggea, *Energy Environ. Sci.*, 2015, **8**, 1905–1922.
47 H. Luo, Q. Gou, Y. Zheng, K. Wang, R. Yuan, S. Zhang, W. Fang, Z. Luogu, Y. Hu, H. Mei, B. Song, K. Sun, J. Wang and M. Li, *ACS Nano*, 2025, **19**, 2427–2443.
48 Y.-Z. Zheng, N.-N. Wang, J.-J. Luo, Y. Zhou and Z.-W. Yu, *Phys. Chem. Chem. Phys.*, 2013, **15**, 18055–18064.
49 B. A. Marekha, O. N. Kalugin, M. Bria and A. Idrissi, *Phys. Chem. Chem. Phys.*, 2015, **17**, 23183–23194.
50 J. T. Arnold and M. G. Packer, *High Resolution Nuclear Magnetic Resonance*, McGraw-Hill Book, New York, 1959.
51 M. N. C. Zarycz and C. F. Guerra, *J. Phys. Chem. Lett.*, 2018, **9**, 3720–3724.
52 K. Hayamizu, S. Tsuzuki, S. Seki and Y. Umebayashi, *J. Phys. Chem. B*, 2012, **116**, 11284–11291.
53 S. Cha, M. Ao, W. Sung, B. Moon, B. Ahlström, P. Johansson, Y. Ouchid and D. Kim, *Phys. Chem. Chem. Phys.*, 2014, **16**, 9591–9601.
54 Y. Zhang, G. Wan, N. H. C. Lewis, J. Mars, S. E. Bone, H.-G. Steinrück, Ma. R. Lukatskaya, N. J. Weadock, M. Bajdich, O. Borodin, A. Tokmakoff, M. F. Toney and E. J. Maginn, *ACS Energy Lett.*, 2021, **6**, 3458–3463.
55 S. A. Katsyuba, E. E. Zvereva, A. Vidis and P. J. Dyson, *J. Phys. Chem. A*, 2007, **111**, 352–370.
56 Y. Chen, Y.-H. Zhang and L.-J. Zhao, *Phys. Chem. Chem. Phys.*, 2004, **6**, 537–542.
57 M. A. Czarnecki, Y. Morisawa, Y. Futami and Y. Ozaki, *Chem. Rev.*, 2015, **115**, 9707–9744.
58 Y. Ikemoto, Y. Harada, M. Tanaka, S. Nishimura, D. Murakami, N. Kurahashi, T. Moriwaki, K. Yamazoe, H. Washizu, Y. Ishii and H. Torii, *J. Phys. Chem. B*, 2022, **126**(22), 4143–4151.
59 B. Czarnik-Matusewicz and S. Pilorz, *Vib. Spectrosc.*, 2006, **40**, 235–245.
60 J. L. Trenzado, Y. Rodríguez, A. Gutiérrez, A. Cincotti and S. Aparicio, *J. Mol. Liq.*, 2021, **334**, 116049.
61 T. Masaki, K. Nishikawa and H. Shirota, *J. Phys. Chem. B*, 2010, **114**, 6323–6331.
62 I. A. Borin and M. S. Skaf, *J. Chem. Phys.*, 1999, **110**, 6412–6420.
63 H. Kovacs and A. Laaksonen, *J. Am. Chem. Soc.*, 1991, **113**, 5596–5605.
64 T. H. G. Saji, J. M. Vicent-Luna, T. J. H. Vlugt, S. Calero and B. Bagheri, *J. Mol. Liq.*, 2024, **401**, 124530.
65 C. D'Agostino, M. D. Mantle, C. L. Mullan, C. Hardacre and L. F. Gladden, *ChemPhysChem*, 2018, **19**, 1081–1088.
66 K. Hayamizu, Y. Aihara, H. Nakagawa, T. Nukuda and W. S. Price, *J. Phys. Chem. B*, 2004, **108**, 19527–19532.
67 V. V. Chaban, I. V. Voroshylova, O. N. Kalugin and O. V. PrezhdoIonic, *J. Phys. Chem. B*, 2012, **116**, 7719–7727.
68 U. Mahanta, D. Kundu, R. P. Venkatesh, S. Sujatha, S. A. Ilangovan and T. Banerjee, *Ind. Eng. Chem. Res.*, 2019, **58**, 22741–22753.
69 P. Tan, J. Yue, Y. Yu, B. Liu, T. Liu, L. Zheng, L. He, X. Zhang, L. Suo and L. Hong, *J. Phys. Chem. C*, 2021, **125**, 11838–11847.
70 M. Zanatta, V. U. Antunes, C. F. Tormena, J. Dupont and F. P. dos Santos, *Phys. Chem. Chem. Phys.*, 2019, **21**, 2567–2571.
71 L. Sun, O. Morales-Collazo, H. Xia and J. F. Brennecke, *J. Phys. Chem. B*, 2015, **119**, 15030–15039.
72 Y. K. J. Bejaoui, F. Philippi, H.-G. Stammler, K. Radacki, L. Zapf, N. Schopper, K. Goloviznina, K. A. M. Maibom, R. Graf, J. A. P. Sprenger, R. Bertermann, H. Braunschweig, T. Welton, N. V. Ignat'ev and M. Finze, *Chem. Sci.*, 2023, **14**, 2200–2214.
73 S. P. Beltran, X. Cao, J.-G. Zhang and P. B. Balbuena, *Chem. Mater.*, 2020, **32**, 5973.
74 S. C. Kim, X. Kong, R. A. Vilá, W. Huang, Y. Chen, D. T. Boyle, Z. Yu, H. Wang, Z. Bao, J. Qin and Y. Cui, *J. Am. Chem. Soc.*, 2021, **143**, 10301.
75 F. Hu, J. Chen, H. Cao, H. Wang, H. Guo and X. Ouyang, *Adv. Funct. Mater.*, 2025, **35**, 2413004.
76 L. Sun, O. Morales-Collazo, H. Xia and J. F. Brennecke, *J. Phys. Chem. B*, 2016, **120**, 5767–5776.
77 A. Noda, K. Hayamizu and M. Watanabe, *J. Phys. Chem. B*, 2001, **105**, 4603–4610.
78 D. R. MacFarlane, M. Forsyth, E. Izgorodina, A. P. Abbott, G. Annat and K. Fraser, *Phys. Chem. Chem. Phys.*, 2009, **11**, 4962–4967.
79 H. Tokuda, S. Tsuzuki, M. A. B. H. Susan, K. Hayamizu and M. Watanabe, *J. Phys. Chem. B*, 2006, **110**, 19593–19600.
80 W. Xu, E. I. Cooper and C. A. Angell, *J. Phys. Chem. B*, 2003, **107**(25), 6170–6178.
81 M. Sevilla, G. A. Ferrero, N. Diez and A. B. Fuertes, *Carbon*, 2018, **131**, 193–200.
82 M. Yu, Y. Lu, H. Zheng and X. Lu, *Chem.–Eur. J.*, 2018, **24**, 3639–3649.
83 L. Demarconnay, E. Raymundo-Piñero and F. Béguin, *Electrochem. Commun.*, 2010, **12**, 1275–1278.
84 M. R. Lukatskaya, S.-M. Bak, X. Yu, X.-Q. Yang, M. W. Barsoum and Y. Gogotsi, *Adv. Energy Mater.*, 2015, **5**, 1500589.
85 K. Kim, Y. Ando, A. Sugahara, S. Ko, Y. Yamada, M. Otani, M. Okubo and A. Yamada, *Chem. Mater.*, 2019, **31**(14), 5190–5196.
86 S. Sayah, A. Ghosh, M. Baaziz, R. Amine, M. Dahbi, Y. Amine, F. Ghamouss and K. Amine, *Nano Energy*, 2022, **98**, 107336.

87 Y. Song, K. Zhang, X. Li, C. Yan, Q. Liu and A. Tang, *J. Mater. Chem. A*, 2021, **9**, 26354–26361.
88 L. Pan, B. Hu, X. Zhu, X. Chen, J. Shang, H. Tan, W. Xue, Y. Zhu, G. Liu and R.-W. Li, *J. Mater. Chem. C*, 2013, **1**, 4556–4564.
89 A. A. Adeniyi, T. L. Ngake and J. Conradie, *Electroanalysis*, 2020, **32**, 2659–2668.
90 M. Shakourian-Fard, G. Kamath, S. M. Taimoory and J. F. Trant, *J. Phys. Chem. C*, 2019, **123**, 15885–15896.
91 P. Peljo and H. H. Girault, *Energy Environ. Sci.*, 2018, **11**, 2306–2309.
92 N. O. Laschuk, E. B. Easton and O. V. Zenkina, *RSC Adv.*, 2021, **11**, 27925–27936.
93 B.-A. Mei, O. Munteshari, J. Lau, B. Dunn and L. Pilon, *J. Phys. Chem. C*, 2018, **122**, 194–206.
94 J. P. A. dos Santos, F. C. Rufino, J. I. Y. Ota, R. C. Fernandes, R. Vicentini, C. J. B. Pagan, L. M. Da Silva and H. Zanin, *J. Energy Chem.*, 2023, **80**, 265–283.
95 J. Zhao, G. Gorbatovski, O. Oll, T. Thomberg and E. Lust, *Electrochim. Acta*, 2019, **319**, 82–87.
96 X. Wang, T. S. Mathis, K. Li, Z. Lin, L. Vlcek, T. Torita, N. C. Osti, C. Hatter, P. Urbankowski, A. Sarycheva, M. Tyagi, E. Mamontov, P. Simon and Y. Gogotsi, *Nat. Energy*, 2019, **4**, 241–248.
97 C. Lei, F. Markoulidis, Z. Ashitaka and C. Lekakou, *Electrochim. Acta*, 2013, **92**, 183–187.